

MACHINE-LEARNING INTERATOMIC POTENTIAL FOR ULTRA-WIDE BANDGAP
SEMICONDUCTOR AND X-RAY SCATTERING STUDY OF CHARGE DENSITY WAVE

A Thesis
Presented to the Faculty of the Graduate School
of Cornell University
In Partial Fulfillment of the Requirements for the Degree of
Master of Science

by
Joyce Christiansen-Salameh
May 2022

© 2022 Joyce Christiansen-Salameh

ABSTRACT

Understanding the role of native defects, impurities, and dopants in reducing the intrinsically high thermal conductivity of wurtzite AlN is of importance for effective thermal management of next-generation devices. A computational approach is pursued that implements a machine-learning interatomic potential (MLP) to transfer the accuracy of first principles methods to the lengthscales accessible by molecular dynamics (MD) simulations. MLPs are trained on a dataset obtained by density functional theory calculations to map atomic configurations to per atom energies, reconstructing the potential energy surface. In this work, a training dataset is generated and two styles of MLP, a neural network potential and a gaussian approximation potential, are trained and evaluated. The established framework for MLPs, which is limited to the consideration of short-range interactions, is not sufficient to reproduce the potential energy surface of wurtzite AlN due to the material's piezoelectric nature.

Transition metal dichalcogenides host charge density wave (CDW) states, a periodic modulation of electron density accompanied by a periodic lattice distortion that emerges below a transition temperature. A signature of the CDW state is the appearance of superlattice reflections in diffraction patterns. Synchrotron source x-ray scattering measurements of bulk 2H-TaSe₂ were taken on a cooling-warming cycle over the range of the commensurate and incommensurate CDW transition temperatures. The modulation vector defining the periodicity of the CDW state exhibited thermal hysteresis, and the commensurate CDW transition shifted on the warming cycle. The persistence of superlattice reflections above the incommensurate transition temperature indicated local ordering prior to the onset of the CDW state.

BIOGRAPHICAL SKETCH

Joyce Christiansen-Salameh was born in the San Francisco Bay Area. She received a B.S. in Materials Science and Engineering with a minor in Computer Science from the University of California, Davis. In her undergraduate studies at UC Davis, she conducted research in Professor Roopali Kukreja's group, which focuses on magnetic and electronic properties of materials. Joyce currently resides in Ithaca, New York where she is a M.S. student in the Materials Science and Engineering department at Cornell University. Joyce is a member of Professor Zhiting Tian's research group, which focuses on nanoscale heat transfer.

ACKNOWLEDGMENTS

I have learned immensely from my advisor, Professor Zhiting Tian. I would like to thank her for investing in my growth as a research scientist and engineer, and for motivating me with her innovative spirit and positive outlook.

Among my labmates in the ZT group I have found teammates, knowledgeable mentors, and friends. Thank you for creating such a fun atmosphere to do research, I always look forward to our Friday meeting activities.

The experimental portion of this work conducted at the Cornell High Energy Synchrotron Source was a team effort of our research group, I would like to emphasize the important contributions from Jinghang Dai, Han Huang, and Gustavo Alvarez-Escalante. The experiment was guided by beamline scientist Dr. Jacob Ruff, who also provided valuable perspectives on the data analysis and results.

Finally, thank you to my parents, for a lifetime of support and encouragement, and to my brothers, Tom and James, for inspiring me to pursue both engineering and higher education.

TABLE OF CONTENTS

<i>ABSTRACT</i>	<i>i</i>
<i>BIOGRAPHICAL SKETCH</i>	<i>ii</i>
<i>ACKNOWLEDGMENTS</i>	<i>iii</i>
<i>TABLE OF CONTENTS</i>	<i>iv</i>
<i>LIST OF FIGURES</i>	<i>v</i>
<i>LIST OF TABLES</i>	<i>vi</i>
<i>Machine-learning potential for wurtzite AlN</i>	<i>1</i>
I. Introduction	1
II. Approach	1
III. Methods	2
A. NNP	3
B. GAP	4
IV. Generation of training data	5
V. Model training	6
A. Force locality test	6
B. NNP	7
C. GAP	9
D. Evaluation	10
VI. Future Work	12
<i>X-ray scattering study of charge density wave in 2H-TaSe₂</i>	<i>13</i>
I. Introduction	13
II. Experimental procedure	14
III. Data analysis	15
IV. Results	17
<i>REFERENCES</i>	<i>19</i>

LIST OF FIGURES

Figure 1: Workflow of training data generation	5
Figure 2: Force locality test	6
Figure 3: Bond length distribution of training data	7
Figure 4: Convergence of n_{\max} , l_{\max}	8
Figure 5: NNP training loss	8
Figure 6: NNP true-predicted curve and residuals	9
Figure 7: GAP true-predicted curve and residuals	10
Figure 8: NNP trained on unstrained configurations	10
Figure 9: hk_0 and $0kl$ planes	14
Figure 10: Fitting of superlattice reflections	15
Figure 11: Fitting results for one reflection.....	16
Figure 12: Example of spurious signal	16
Figure 13: Relative intensity over temperature cycle.....	17
Figure 14: q_{CDW} over temperature cycle.....	17

LIST OF TABLES

Table 1: R^2 and RSME values of NNP	8
Table 2: R^2 and RSME values of GAP	9

Machine-learning potential for wurtzite AlN

I. Introduction

The wurtzite phase of AlN is an ultra-wide bandgap semiconductor with prospects in power electronics, radio frequency (RF) technologies, and deep ultraviolet (UV) photonics. The high thermal conductivity of AlN is a distinct advantage given continued trends towards high power drive and compact architectures that exacerbate thermal loads. Experimental measurements of AlN report thermal conductivity as high as $320 \text{ Wm}^{-1}\text{K}^{-1}$ at room temperature¹, matching theoretical predictions for a perfect bulk single crystal^{2,3}. However, native defects and impurities, or intentional dopants, are known to greatly reduce the thermal conductivity of semiconductors by acting as scattering sites for phonons, the primary heat carrier in non-metallic solids. The single crystal growth process unavoidably results in substitutional impurities (O, C, and Si atoms), Al and N vacancies, and dislocation lines, the levels of which are more pervasive in thin film AlN. Experimentally, it is difficult to both control and characterize defect and impurity concentrations in physical samples, and thus study the fundamental impacts on thermal conductivity. This task is better suited to a computational approach, which offers exact control of the system on the atomic level. The ultimate goal of this work is to develop a computational framework that facilitates a deeper understanding of how defects and impurities effect the thermal properties of AlN.

II. Approach

First principles calculations, such as density functional theory (DFT), treat electron and nuclei interactions explicitly as governed by the laws of quantum mechanics, and can predict accurately materials properties. However, due to polynomial scaling of computational demand with system size, these calculations are limited practically to systems with a few hundred atoms and on picosecond timescales⁴. Consider AlN with a point defect concentration of $5 \times 10^{19} \text{ cm}^{-3}$.

Representing a single vacancy cluster would require a simulation cell with $\sim 2,000$ atoms, violating the constraints. Similarly, dopant concentrations for typical applications of AlN range from $\sim 10^{15}$ cm^{-3} for drift regions in power electronics, to $\sim 10^{21}$ cm^{-3} for opto-electronics⁵.

On the other hand, molecular dynamics (MD) simulations can handle systems with up to 10^5 - 10^6 atoms and millisecond timescales. MD simulations are governed by a reconstruction of the potential energy surface (PES). At each timestep, the potential is queried for per atom energies as a function of atomic positions. The energies and the gradient of the potential, the atomic forces, are used to update the simulation according to classical equations of motion. The PES is typically reconstructed via analytical functions, which can describe the qualitative behavior of the system but suffer from low quantitative accuracy. For example, the widely used Tersoff and Stillinger-Weber potentials produce 35% and 210% error in forces for Si compared to first principles methods⁶. Machine learning potentials (MLP) trained on *ab initio* data bridge the gap between first principles accuracy and the time and lengthscales accessible by MD. For example, a general-purpose Si MLP reproduced energies within 1 meV of DFT data, which is less typical discrepancies between DFT codes themselves⁷. This method has already proven effective for ultra-wide bandgap semiconductors, a MLP for $\beta\text{-Ga}_2\text{O}_3$ was used to calculate anisotropic thermal conductivity with good agreement to experimental values⁸. The workflow of developing a MLP consists of obtaining first principles training data, selecting model hyperparameters, training the model, and evaluating accuracy.

III. Methods

MLPs map atom-centered descriptors to per atom energies, though first principles calculations output the total energy of the system. A core assumption is that the total energy can be expressed as a sum of individual atomic energies. MLPs include additional quantities of per atom forces and

virial, which are also output by first principles methods and can be found with the energy derivative, to reinforce proper allotment of energy per atom. Another assumption is that of locality. An atomic descriptor encodes in vector form the *local* environment of each atom in a configuration, such that the representation is invariant to translation, rotation, and the exchange of equivalent atoms. Short-range interatomic interactions are captured for the set of atoms within a cutoff radius, and long-range contributions such as Coulomb and van der Waals forces are assumed to be effectively zero.

Two styles of MLPs, a neural network potential (NNP) and a gaussian approximation potential (GAP) are selected to reconstruct the PES of AlN. A brief overview of each is given below, the full formalisms of the NNP and GAP models can be found in *Yanxon et. al 2021* and *Bartok et. al 2018*, respectively^{7,9}.

A. NNP

The NNP is a feed-forward neural network that minimizes the discrepancies between predicted and DFT calculated energies, forces, and stresses. A simplified version of the loss function for a system with one atom is written in **Equation 1**, where M is the number of training configurations, N_{atom}^i is the number of atoms in the i th configuration, β_F and β_S are force and stress coefficients that determine contribution relative to the energy term, and Δ_p is a regularization penalty on the weights to prevent overfitting. Forces are obtained by applying the chain rule to calculate the analytic derivative of the energy at each atomic position. The stress tensor is calculated by the virial stress relation.

$$\Delta = \frac{1}{2M} \sum_{i=1}^M \left[\left(\frac{E_i - E_i^{DFT}}{N_{atom}^i} \right)^2 + \frac{\beta_F}{3N_{atom}^i} \sum_{j=1}^{3N_{atom}^i} (F_{ij} - F_{ij}^{DFT})^2 + \frac{\beta_S}{6} \sum_{p=0}^2 \sum_{q=0}^p (S_{pq} - S_{pq}^{DFT})^2 \right] + \Delta_p \quad (1)$$

NNP models in this work implemented a smooth SO(3) power descriptor, which is an expansion of an atomic neighbor density function in terms of spherical harmonics and a radial basis¹⁰. The key parameters of the SO(3) descriptor are the cutoff radius, the number of spherical harmonic terms l_{\max} and the number of radial terms n_{\max} . The PyXtal-FF package provided the infrastructure for calculating descriptors and training the NNP models⁹.

B. GAP

GAP models express the total energy as a summation over kernel basis functions as written in **Equation 2**, where K , the kernel or covariance function, is a similarity measure of atomic descriptors of neighborhoods R_i and R_j . Sparsity is implemented by calculating the kernel on a subset of M representative points. CUR matrix decomposition identifies representative points by maximum dissimilarity.

$$E = \sum_i \sum_j^M \alpha_s K(R_i, R_j) \tag{2}$$

The GAP models in this work combined a 2-body potential with a many-body Smooth Overlap of Atomic Positions (SOAP) kernel. The model is trained by a regularized least squares fit of the weights α_s to first principles quantities, as written in **Equation 3**. For a dataset with N configurations, matrix y has D components corresponding to total energies, forces, and virial stress terms, and matrix y' contains the unknown energies per atom. L is the linear differential operator of size $N \times D$ such that $y = Ly'$. K_{MM} is the kernel matrix of the M representative points, K_{MN} is the kernel matrix of the representative set and the training data, and Λ^{-1} contains the weights on input values. The kernel regression is equivalent to a Gaussian process.

$$\alpha_s^* = [K_{MM} + (LK_{MN})^T \Lambda^{-1} LK_{MN}]^{-1} (LK_{MN})^T \Lambda^{-1} y \tag{3}$$

GAP models in this work were trained using the GAP extension of the QUIP package^{11,12}.

IV. Generation of training data

An initial training dataset was obtained from *ab initio* molecular dynamics (AIMD) simulations conducted with the Vienna *Ab initio* Simulation Package (VASP) and using a Perdew–Burke-Ernzerhof (PBE) pseudopotential. The relaxed lattice parameters of the wurtzite AlN structure ($a=3.13 \text{ \AA}$ and $c=5.02 \text{ \AA}$) were in good agreement with experiment¹³. The simulation cell consisted of a 2x2x4 supercell containing 128 atoms total. AIMD simulations at 300, 500, 700, 900 and 1100 K were run in the NVT ensemble with a 1 fs timestep for a total of 2 ps. Plane wave basis sets with an energy cutoff of 800 eV and the Γ -point approximation were applied. Atomic configurations and the corresponding total energies, forces, and virials were sampled from the AIMD trajectories every 40 fs to avoid correlation, accumulating 250 training data points.

A preliminary NNP was trained for use in MD simulations to generate the remainder of the training data. Sampling trajectories from MD reduces computational cost, accesses longer timescales, and provides a more representative set of configurations. Note that the simulation cell employs the lattice parameters determined by DFT relaxation at 0K and is held at constant volume in the NVT ensemble. MD simulations were conducted on supercells modified by isotropic strain to include in the training set configurations that reflect changes in volume during equilibration and

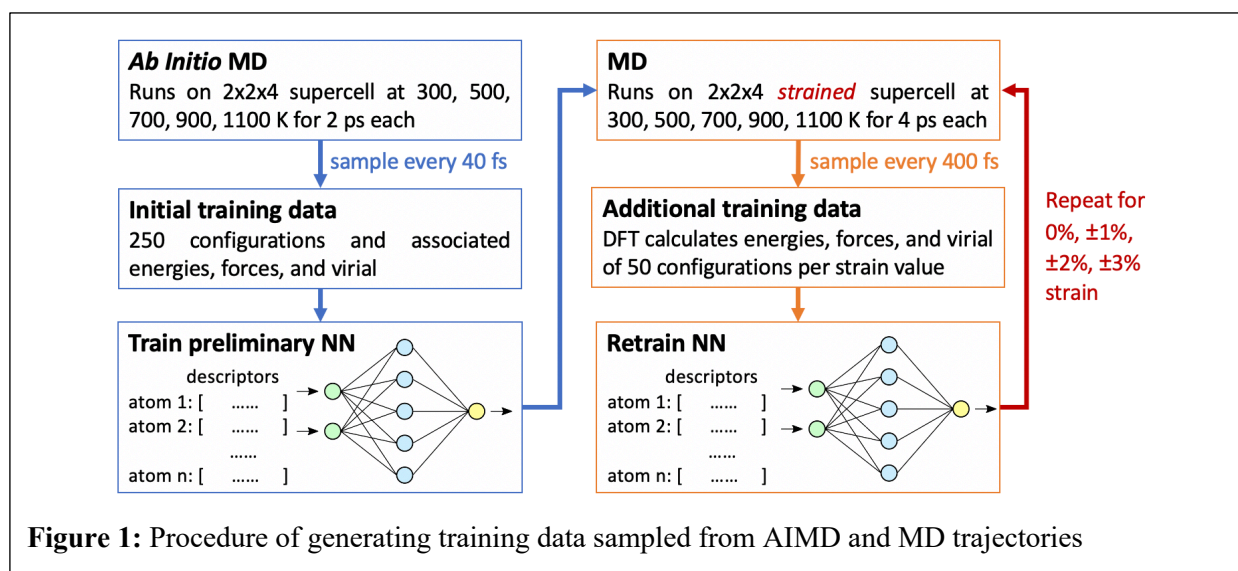


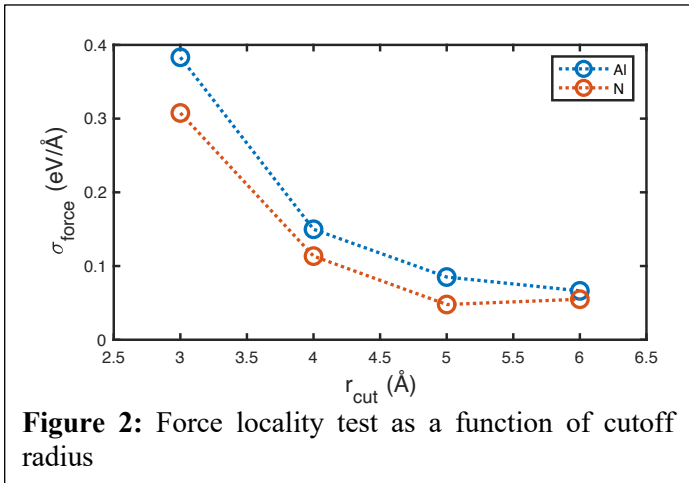
Figure 1: Procedure of generating training data sampled from AIMD and MD trajectories

at finite temperatures, and a sampling of various bond lengths. **Figure 1** outlines the procedure of generating the training data. Strains from 0% to $\pm 3\%$ were applied to the supercell in increments of $\pm 1\%$. At each temperature, an MD simulation was run with the Large-scale Atomic/Molecular Massively Parallel Simulator (LAMMPS) in the NVT ensemble with a timestep of 1 fs for a total of 4 ps. For each increment of strain, configurations from the MD trajectories at each temperature were sampled every 400 fs, the energies, forces, and virials of the sampled configurations were calculated with DFT using the same parameters as the previous AIMD runs, and the NNP was retrained with the additional training data. This process resulted in 350 data points, which in combination with the initial training dataset totaled 600 training data points.

V. Model training

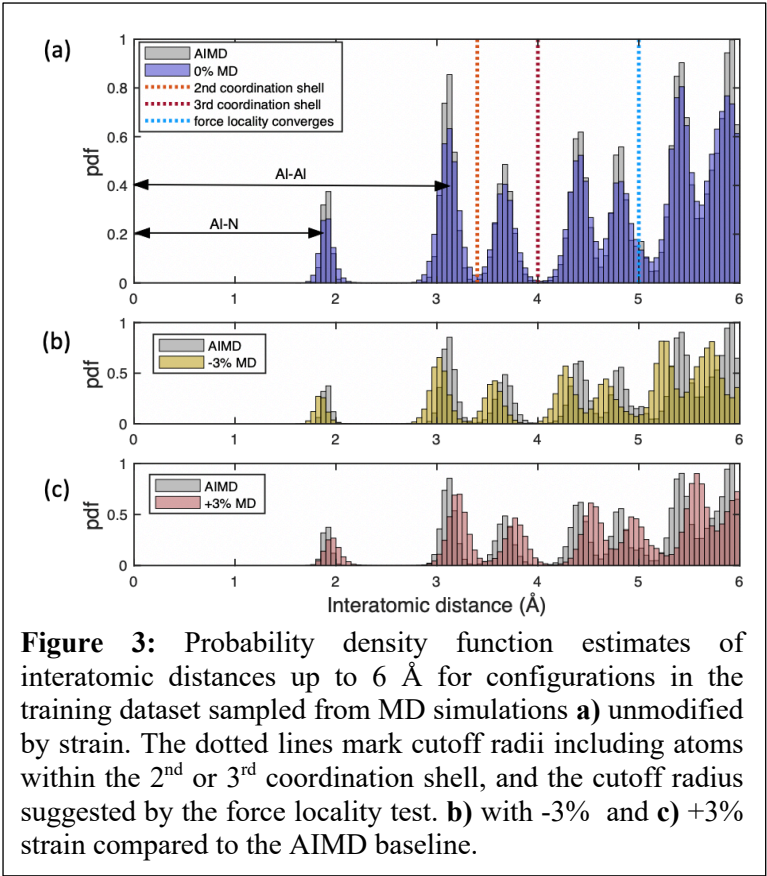
A. Force locality test

The cutoff radius of the atomic descriptor must be large enough to include all atoms that contribute significantly to short-range interactions, but also must be minimized to reduce the computational expense of encoding atomic configurations both during model training



and MD simulations. A force locality test can inform the accuracy of a given cutoff radius¹⁴. Within a simulation cell, one atom was selected. A set of configurations was generated by randomly perturbing atoms outside of the sphere defined by the cutoff radius. The perturbations were small, with a standard deviation of ~ 1 Å. The forces on the central atom were solved by DFT, and the standard deviation of the change from the unperturbed configuration was calculated. The test was

repeated for atoms occupying each of the four positions of the AlN unit cell. The locality test converges near 5 Å for forces on both Al and N atoms (**Figure 2**). Note that while the locality test can assess the accuracy arising from short-range interactions, it cannot distinguish long-range contributions that are included in DFT calculations via periodic boundary conditions, and does not apply to strong polar interactions¹⁴.

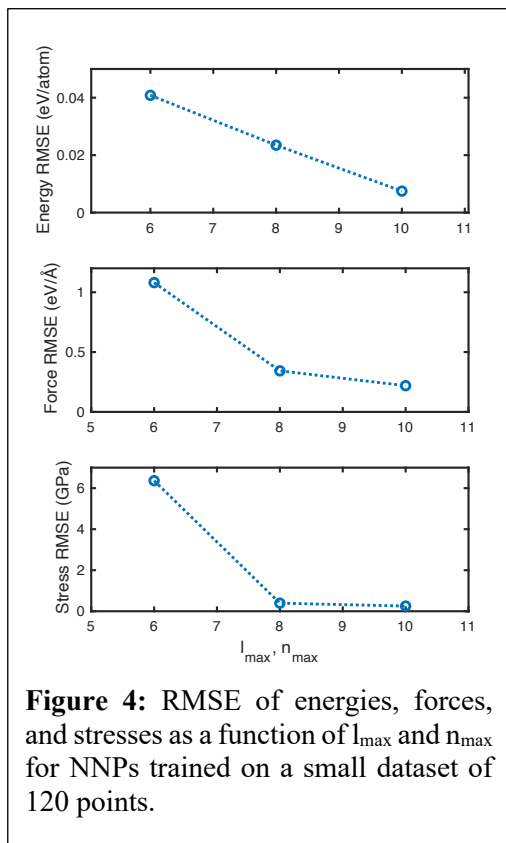


Guidelines suggest including up to the 2nd or 3rd coordination shell within the cutoff radius. However, the force locality test indicates this is not sufficient for AlN. **Figure 3a** shows the distribution of interatomic distances in the training dataset configurations unmodified by strain, and gives a picture of which interactions are included for different choices of cutoff radius. The shifts of interatomic distances for the two extremes of the training dataset, configurations modified by -3% and +3% isotropic strain, are shown in **Figure 3b-c**.

B. NNP

The data was split 80/20 into training and testing sets such that each set contained an equal distribution of configurations sampled from the various strains and temperatures. An SO(3) descriptor with $r_{\text{cut}} = 5.0$ Å, $l_{\text{max}} = 8$, and $n_{\text{max}} = 8$ transformed configurations to input vectors. A

test examining the performance of NNPs trained on a small dataset of 120 points and varying l_{\max} and n_{\max} of the SO(3) descriptor indicates the choice of $l_{\max}=8$ and $n_{\max}=8$ is adequate to describe the atomic environment (**Figure 4**). The architecture of the NNP consisted of 4 hidden layers with 120 nodes each and a linear output layer. The network architecture was refined by the grid search method. Nonlinearity was introduced by a ReLU activation function at each hidden layer. The force and stress coefficients of the loss function were set to 0.03 and 0.005, respectively. The model was trained with a batch size of 256, an Adam optimizer, and a 10^{-3} learning



rate for 150 epochs, at which training loss converged (**Figure 5**). R^2 and root mean-squared error (RMSE) values are listed in **Table 1**. True-predicted curves and the residuals of energy, force, and stress are shown in

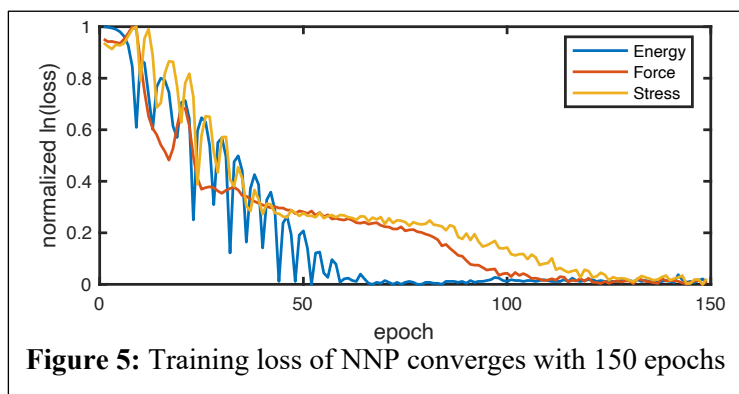
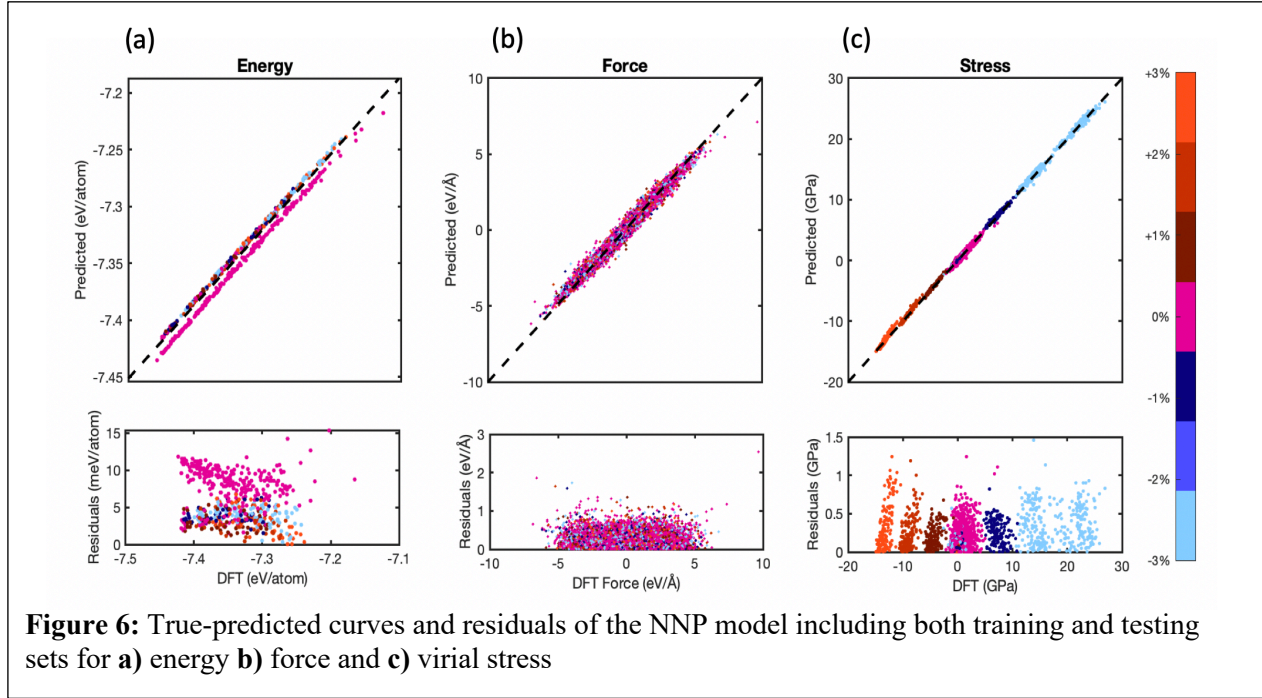


Figure 6.

Table 1: R^2 and RMSE values of NNP model

	Energy		Force		Stress	
	R^2	RMSE (meV/atom)	R^2	RMSE (eV/ Å)	R^2	RMSE (GPa)
Train	0.981	6.57	0.980	0.154	0.999	0.244
Test	0.978	6.13	0.981	0.150	0.999	0.233

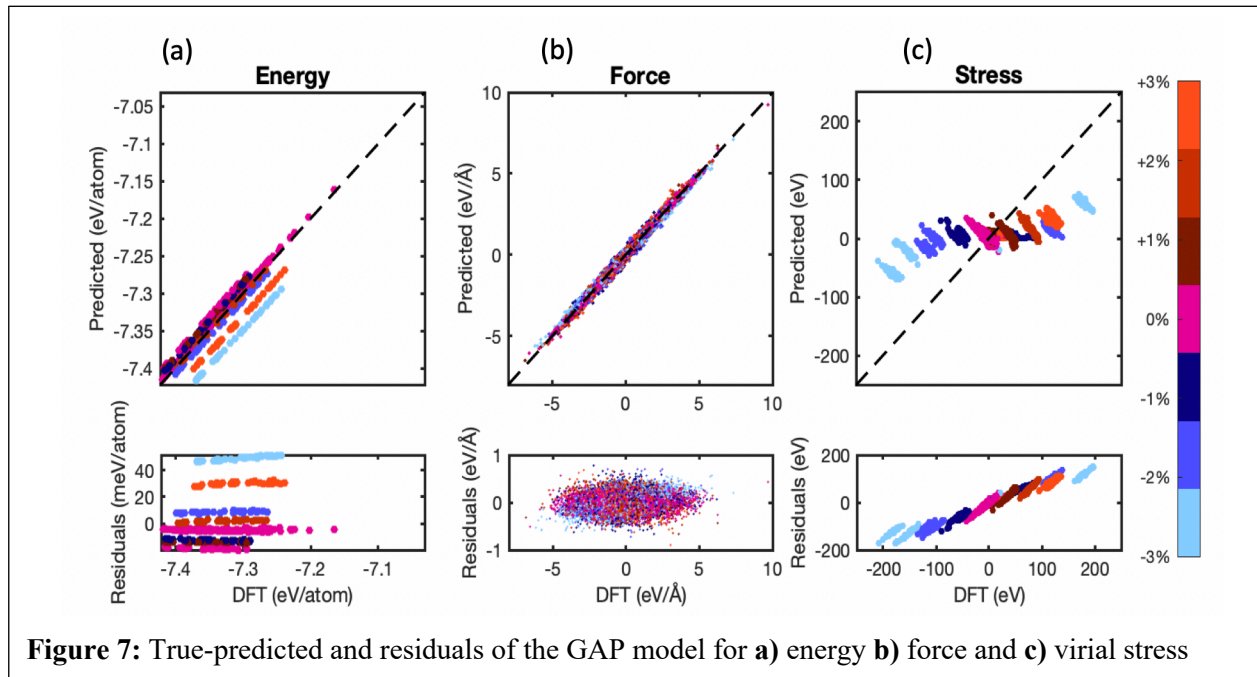


C. GAP

A GAP model was trained. The 2-body term had a cutoff radius of 5.5 \AA and $M = 15$ representative points chosen by uniform selection. The SOAP kernel had a cutoff radius of 5.5 \AA and n_{\max} and l_{\max} were set to 10. CUR matrix decomposition was applied to select $M = 200$ representative points. Other SOAP kernel parameters were $\zeta = 4$, $\delta = 3.5 \text{ eV}$, and smearing parameter $\sigma_{\text{atom}} = 0.5 \text{ \AA}$. The default standard deviations of the energy, force, and stress data were 0.001 eV/atom , 0.01 eV/\AA , and 0.05 eV , respectively. **Table 2** contains the R^2 and RMSE values of the GAP training and testing sets. The true-predicted curves and residuals of energy, stress, and force are shown in **Figure 7**.

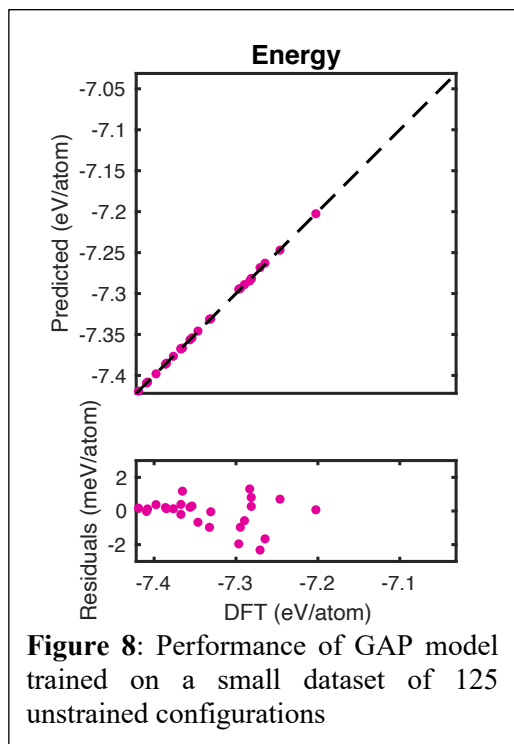
Table 2: R^2 and RMSE values of GAP model

	Energy		Force		Stress	
	R^2	RMSE (meV/atom)	R^2	RMSE (eV/Å)	R^2	RMSE (eV)
Train	0.835	4.43	0.992	0.325	0.530	1.346
Test	0.877	4.15	0.981	0.410	0.022	2.269



D. Evaluation

The NNP achieves the target accuracy, reproducing energies within 10% of DFT values. However, both the NNP and GAP models demonstrate a strong dependence of residual error on the isotropic strain of the simulation cell. The persistence of this trend with various parameters defining the descriptors (n_{\max} , l_{\max}), NNP (number of hidden layers and nodes, activation function, force and stress coefficients, epochs), and GAP (number of representative points, target standard deviations), as well as the excellent performance of the models for a dataset composed of unstrained



configurations (**Figure 8**), indicates the dependence is not an artifact of a poorly conditioned model. The presence of such offsets from the true-predicted line is a sign of a “missing variable”. The more exaggerated dependence on strain of the GAP model errors could be attributed to a difference in feature space, the GAP model makes predictions based on similarity, while the NNP model uses the descriptors themselves.

Recall the assumption that long-range electrostatic contributions are zero. The tetrahedron formed by Al and adjacent N atoms is non-ideal and there exists a separation of positive and negative charges along the c-axis. As a result, wurtzite AlN exhibits a large spontaneous polarization as well as a piezoelectric polarization controlled by the distance between Al and N ions along the c-axis¹⁵. In a polar lattice, optical phonon mode splitting is determined by the Born effective charge of the ions and the Coulomb interaction screening¹⁶. The magnitude of LO-TO splitting compared to the gap between acoustic A_1 and E_1 modes is indicative of the relative contributions of long-range electrostatic forces and short-range interatomic anisotropy¹⁷. In the unstrained state of AlN, LO-TO splitting is more prominent than $A_1 - E_1$ splitting¹⁸, highlighting the need to address long-range contributions in the model. Furthermore, the magnitude of optical phonon mode splitting has been shown to change with uniaxial and biaxial strain¹⁹. This leads to two possible conclusions 1) In the unstrained state, short-range interactions which are fully captured by the MLPs dictate per atom energies. In strained states, long-range contributions become more significant and are not included in the model, leading to poor performance. 2) In the unstrained state, long-range contributions arising from the spontaneous polarization of AlN are significant, but the model is able to learn some baseline electrostatic contribution. This baseline is no longer universal when data points from strained configurations are added. The evidence for the

latter conclusion is stronger, considering AlN the prominence of optical over acoustic phonon mode splitting.

Accuracy is critical to thermal conductivity calculations. Even potentials that can successfully predict other materials properties, such as the phonon dispersion, may fail to model thermal conductivity. Established methods for developing MLPs based on the locality assumption are not suitable for wurtzite AlN due to its polarizability, therefore a potential that addresses long-range electrostatic contributions must be pursued.

VI. Future Work

The next steps of this work begin with selecting a strategy to include long-range electrostatic contributions in the model, augmenting the MLP framework. One approach for piezoelectric materials is to train a NNP without accounting for long-range contributions and implementing an extremely large cutoff radius. However, the model will only be able to reproduce the contributions of long-range interactions from the local pictures of a uniform strain on the simulation cell. Simply extending the cutoff radius would not be an effective approach for studying defects in AlN. Crystalline defects create local distortions, while an increased cutoff radius can only capture the long-range effects of periodic distortions. Other approaches include adding an electrostatic baseline to the GAP model, or combining a MLP for short-range interactions with a separate, long-range electrostatic model.

Upon successful demonstration of an accurate model and thermal conductivity calculation for pure AlN, the model will be retrained with first principles data of configurations that include defects.

X-ray scattering study of charge density wave in 2H-TaSe₂

I. Introduction

Transition metal dichalcogenides (TMDs) host a rich landscape of electronic states, including charge density wave (CDW) ordering. The CDW state is a long-range modulation of electron density coupled to a periodic distortion of the crystal lattice that emerges below a transition temperature, T_{CDW} . CDW states have potential applications in ultrafast electronics and optics, and are also of interest for their relation to superconductivity. Despite belonging to the same family, TMDs display a variety of CDW ordering, and the origin of the CDW remains under debate²⁰. Proposed mechanisms include the Fermi surface nesting, electron-phonon coupling, and excitonic insulator models²¹.

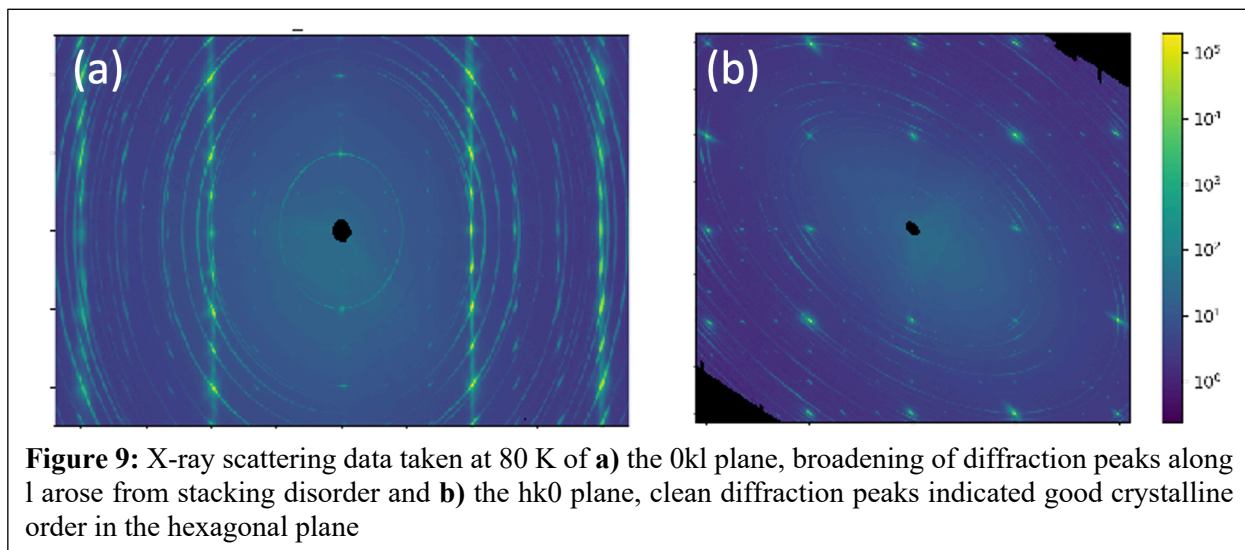
Bulk 2H-TaSe₂ was selected to study CDW in TMDs. 2H-TaSe₂ has hexagonal D_{4h} symmetry in the undistorted phase with lattice constants $a = 3.45 \text{ \AA}$ and $c = 12.7 \text{ \AA}$. The compound is metallic at room temperature, and transitions to an incommensurate (I) CDW state at 122 K and a commensurate (C) CDW state at 90 K upon cooling. The periodicity of the CDW state is defined by the modulation vector, q_{CDW} . Bulk 2H-TaSe₂ has a CDW described by three modulation vectors of hexagonal symmetry and equal magnitude, $|q_{CDW}| = ([1 - \delta(T)]/3)a^*$ where δ is the incommensurability^{22,23}.

A signature of the CDW state is the appearance of superlattice reflections as weak satellite peaks in diffraction patterns. In particular, x-rays are sensitive to the ionic displacements induced by the CDW state. The satellite peaks are located at positions $Q = \tau \pm q_{CDW}$ in reciprocal space, where τ are the integer indices, h, k, l of lattice Bragg peaks²⁴. This work seeks to characterize the temperature-dependence of the CDW modulation vector as a piece of a larger, in-progress study

utilizing additional techniques of inelastic x-ray scattering and thermal conductivity measurements.

II. Experimental procedure

2H-TaSe₂ samples were provided by Professor Robert Cava's group at Princeton. Samples were inspected optically to identify candidates with large single-crystal domains and flat faces. Selected crystals were mounted on polymer loops with GE varnish. Pre-screening of the samples indicated the crystals were well-ordered along a^* and b^* , but broadening of the diffraction peaks along c^* revealed stacking disorder. **Figure 9** shows the $hk0$ and $0kl$ planes of the sample which gave the cleanest signal and was selected for further measurements. Powder rings arose from surface residue, likely a byproduct of the growth process.



High density reciprocal space mapping (HDRM) was performed at beamline 4b of the Cornell High Energy Synchrotron Source (CHESS). This is a synchrotron source technique that rapidly collects volumetric elastic x-ray scattering data over a vast region of reciprocal space. The sample was mounted to a Huber diffractometer and rotated 360° incrementally along three principle axes. At each increment a diffraction pattern was recorded by a PILATUS 6M detector. In post, the hundreds of scans were stitched together to obtain a volumetric dataset with q -resolution of 0.01

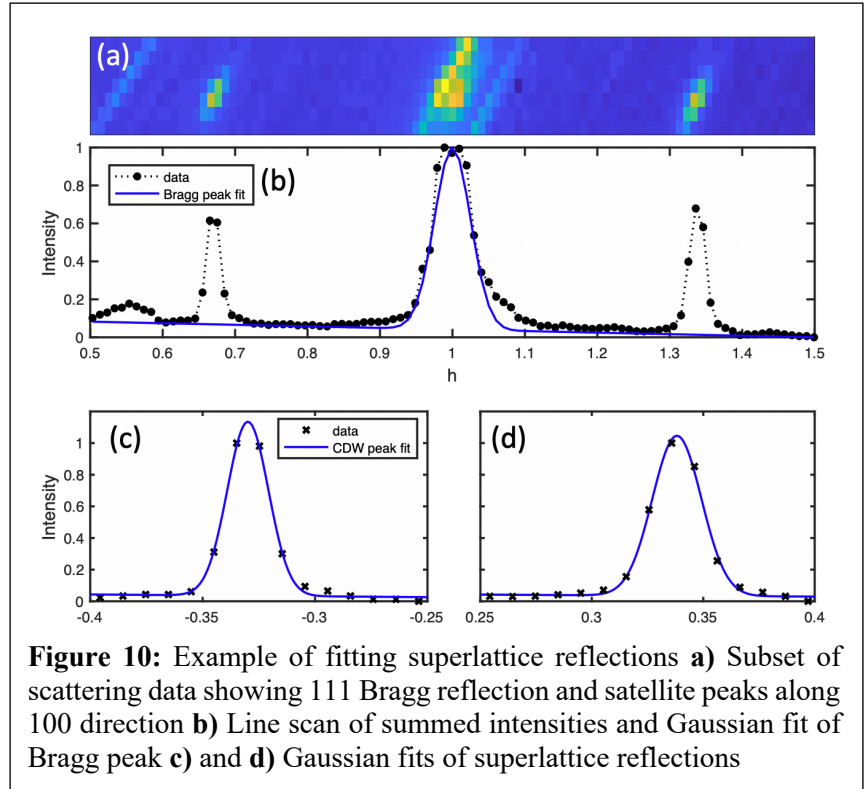
\AA^{-1} . The beam energy was 30 keV and the spot size was 200 x 500 microns. Sample temperature was controlled with a gas cryocooler using liquid Nitrogen to cool from RT to 90 K, and liquid Helium to access temperatures 90K and below. Data was collected at 130, 125, 120, 115, 105, 95, 90, 85, and 80 K. To include the thermal hysteresis behavior, the temperatures were measured on a cooling and warming cycle. The sample was held at 75 K prior to commencing the warming leg of the cycle at 80 K.

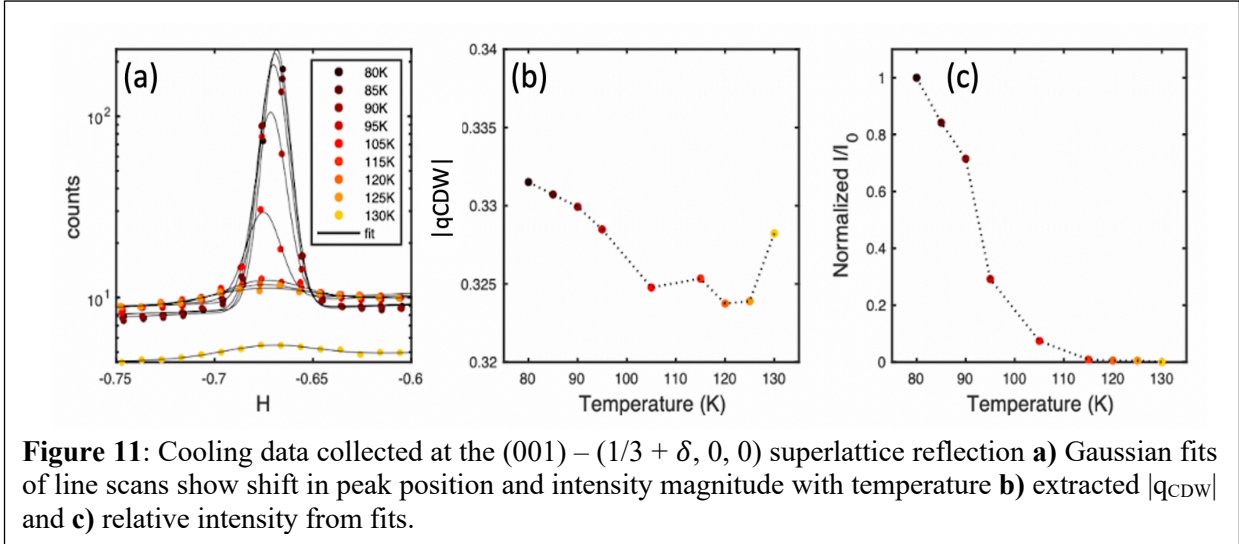
III. Data analysis

For each measured temperature on the cooling and warming cycle, a volumetric dataset was generated containing hundreds of Bragg diffraction peaks and their associated superlattice reflections. Due to a small error in the orientation matrix, hkl indices did not align exactly with Bragg diffraction spots. The error was corrected by fitting the Bragg peak of interest and the two adjacent along the q_{CDW}

direction, and adjusting such that the fitted peak locations were at integer indices.

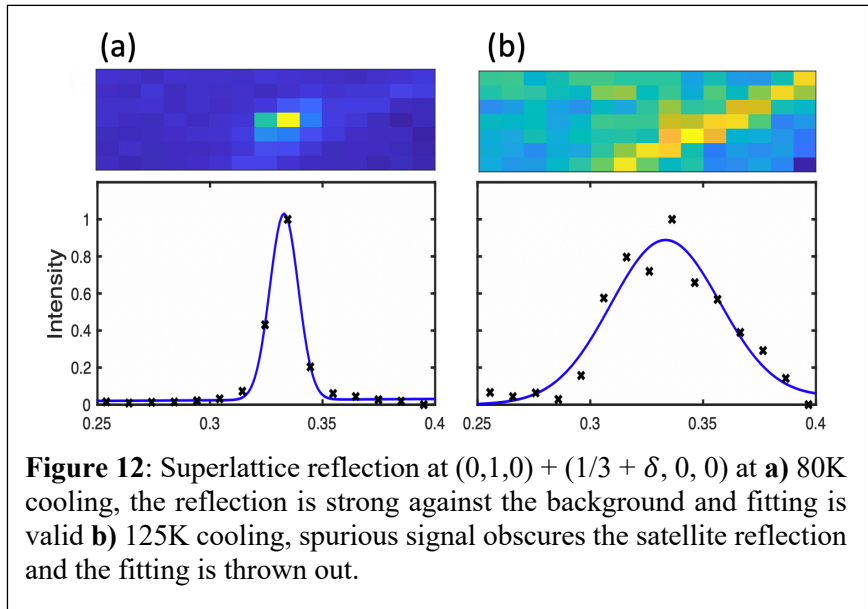
Figure 10 shows a representative fitting of the superlattice reflections located at $(111) \pm (1/3 + \delta, 0, 0)$ and measured at 80 K cooling. A slice of the x-ray scattering data in the hkl





plane was taken along the q_{CDW} direction with a height of 11 pixels centered on the Bragg peak **(10a)**. The slice was summed to produce a line scan along the q_{CDW} direction **(10b)**. The regions surrounding the two superlattice reflections were isolated, and the peaks are fit to a Gaussian with a linear background **(10c-d)**. The relative intensity and q_{CDW} values are extracted from the fits of the Bragg and satellite peaks. The cooling curve evolution of the superlattice reflection located at $(111) - (1/3 + \delta, 0, 0)$ and the extracted values are shown in **Figure 11**.

Superlattice reflections were fit within a subset of the datasets containing 27 Bragg diffraction peaks. Above 115 K superlattice reflections become very weak and may be obscured by intersecting powder diffraction rings **(Figure 12)**. A manual check was conducted to throw out satellite peaks overlapped by spurious signals.



IV. Results

The progression over the cooling and warming cycle of $|q_{CDW}|$ collected from the data subsets is shown in **Figure 13**. To capture the relative intensity, 11 Bragg peaks were selected such that the associated CDW satellites were unobscured throughout the temperature range, the average of the satellite peak intensity relative to the Bragg peak intensity and normalized by the values over the temperature cycle are shown in **Figure 14**.

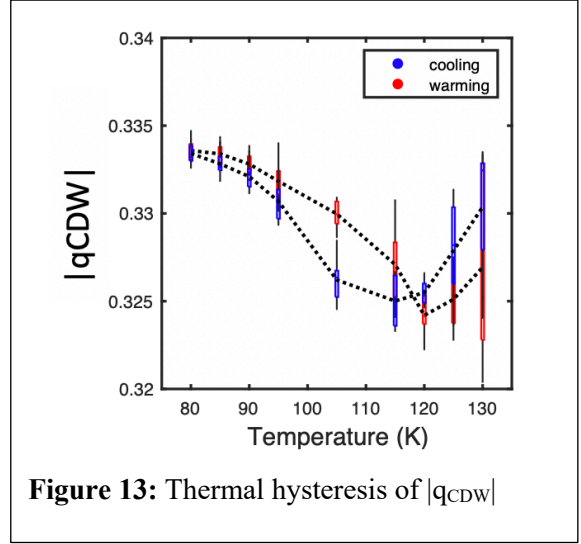


Figure 13: Thermal hysteresis of $|q_{CDW}|$

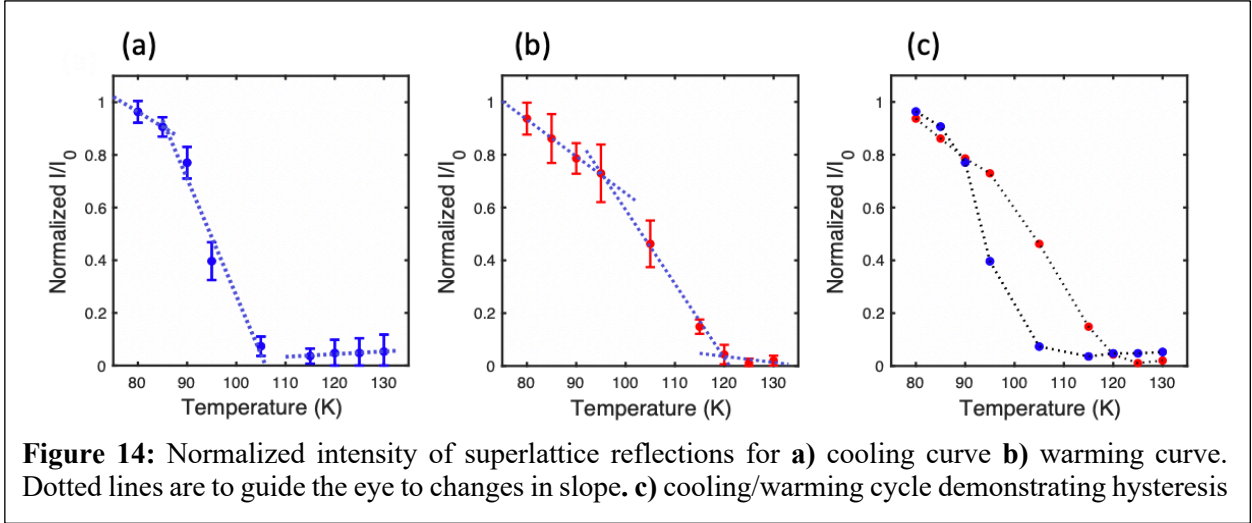


Figure 14: Normalized intensity of superlattice reflections for **a)** cooling curve **b)** warming curve. Dotted lines are to guide the eye to changes in slope. **c)** cooling/warming cycle demonstrating hysteresis

We observed several behaviors consistent with the findings of *Fleming et al. 1980*, who conducted the first x-ray investigation of CDW in bulk $2H-TaSe_2$ ²³. 1) There is a thermal hysteresis in the intensity and the modulation vector. Thermal hysteresis is common among materials exhibiting CDW, and is accompanied by hysteresis in electrical resistance. 2) The commensurate transition temperatures shifts from 90K cooling to ~95K warming. Crystalline defects have been shown to suppress CDW transition temperatures, though this is not the case for our sample despite

stacking disorder. *Fleming et al.* also observed the emergence of a striped CDW state defined by one commensurate and two incommensurate modulation vectors between 93 and 112 K of the warming cycle. The q-resolution of our data was not high enough to observe the peak splitting indicative of the striped phase. Similarly to *Petkov et al., 2020*, CDW satellite peak signal is detected above the 122 K transition temperature, indicating the onset of local ordering prior to the long-range periodic ordering of the CDW state²⁴.

The results of this work confirm the CDW transition temperatures of our selected sample, despite stacking disorder, and give the temperature dependence of the modulation vector magnitude. In future work, findings will inform temperature-dependent behaviors of the phonon dispersion and thermal conductivity.

REFERENCES

1. Cheng, Z. *et al.* Experimental observation of high intrinsic thermal conductivity of AlN. *Phys. Rev. Mater.* **4**, (2020).
2. Slack, G. A., Tanzilli, R. A., Pohl, R. O. & Vandersande, J. W. The intrinsic thermal conductivity of AlN. *J. Phys. Chem. Solids* **48**, 641–647 (1987).
3. Lindsay, L., Broido, D. A. & Reinecke, T. L. Ab initio thermal transport in compound semiconductors. *Phys. Rev. B - Condens. Matter Mater. Phys.* **87**, 165201 (2013).
4. Schuch, N. & Verstraete, F. Computational complexity of interacting electrons and fundamental limitations of density functional theory. (2009) doi:10.1038/NPHYS1370.
5. Harris, J. S. *et al.* On compensation in Si-doped AlN. *Appl. Phys. Lett.* **112**, 152101 (2018).
6. Rohskopf, A., Seyf, H. R., Gordiz, K., Tadano, T. & Henry, A. Empirical interatomic potentials optimized for phonon properties. *npj Comput. Mater.* **2017 31 3**, 1–7 (2017).
7. Bartók, A. P., Kermode, J., Bernstein, N. & Csányi, G. Machine Learning a General-Purpose Interatomic Potential for Silicon. *Phys. Rev. X* **8**, 041048 (2018).
8. Li, R. *et al.* A deep neural network interatomic potential for studying thermal conductivity of β -Ga₂O₃. *Appl. Phys. Lett.* **117**, (2020).
9. Chomiuk, L. *et al.* PyXtal_FF: a python library for automated force field generation The Proper Motion of Pyxis: The First Use of Adaptive Optics in Tandem with HST on a Faint Halo Object This content was downloaded from IP address 67 OPEN ACCESS RECEIVED PyXtal_FF: a python library for automated force field generation. *Mach. Learn. Sci. Technol* **2**, 27001 (2021).
10. Bartók, A. P., Kondor, R. & Csányi, G. On representing chemical environments. *Phys. Rev. B* **87**, 184115 (2013).
11. Bartók, A. P., Payne, M. C., Kondor, R. & Csányi, G. Gaussian Approximation Potentials: The Accuracy of Quantum Mechanics, without the Electrons. (2009) doi:10.1103/PhysRevLett.104.136403.
12. GitHub - libAtoms/QUIP: libAtoms/QUIP molecular dynamics framework: <http://www.libatoms.org>.
13. Kröncke, H., Kröncke, K., Figge, S., Epelbaum, B. M. & Hommel, D. Determination of the Temperature Dependent Thermal Expansion Coefficients of Bulk AlN by HRXRD. **114**, (2008).
14. Deringer, V. L. & Csányi, G. Machine learning based interatomic potential for amorphous carbon. *Phys. Rev. B* **95**, 094203 (2017).
15. Fei, C. *et al.* AlN piezoelectric thin films for energy harvesting and acoustic devices. *Nano Energy* **51**, 146–161 (2018).
16. Wang, H., Xie, Y., Li, Y. & Zhang, N. Dependence of the Structure, Optical Phonon Modes and Dielectric Properties on Pressure in Wurtzite GaN and AlN. *Adv. Mater. Phys. Chem.* **05**, 1302–1308 (2015).
17. Tütüncü, H. & Srivastava, G. Phonons in zinc-blende and wurtzite phases of GaN, AlN, and BN with the adiabatic bond-charge model. *Phys. Rev. B - Condens. Matter Mater. Phys.* **62**, 5028–5035 (2000).
18. Wang, H., Jin, G. & Tan, Q. Lattice dynamics and elastic properties of wurtzite aln and gan. *Proc. - 2020 3rd Int. Conf. Adv. Electron. Mater. Comput. Softw. Eng. AEMCSE*

- 2020 606–610 (2020) doi:10.1109/AEMCSE50948.2020.00132.
19. Wagner, J.-M. & Bechstedt, F. Properties of strained wurtzite GaN and AlN: Ab initio studies. doi:10.1103/PhysRevB.66.115202.
 20. Lin, D. *et al.* Patterns and driving forces of dimensionality-dependent charge density waves in 2H-type transition metal dichalcogenides. *Nat. Commun.* **11**, (2020).
 21. Xu, Z. *et al.* Topical review: recent progress of charge density waves in 2D transition metal dichalcogenide-based heterojunctions and their applications. *Nanotechnology* **32**, 492001 (2021).
 22. Moncton, D. E., Axe, J. D. & Disalvo, F. J. Neutron scattering study of the charge-density wave transitions in 2H-TaSe₂ and 2H-NbSe₂. **16**, (1977).
 23. Chang, C. C. *et al.* Broken Hexagonal Symmetry in the Incommensurate Charge-Density Wave Structure of 2H-TaSe₂. *Phys. Rev. Lett* **45**, 4330 (1980).
 24. Petkov, V., Chapagain, K., Shastri, S. & Ren, Y. Genesis of the periodic lattice distortions in the charge density wave state of 2H-TaSe₂. *Phys. Rev. B* **101**, 121114–121115 (2020).